



Use of Geogrid for Improved Performance of Ballasted Tracks: Experimental and DEM Approaches

Trung Ngo¹ · Buddhima Indraratna^{2,3}

Received: 14 December 2023 / Accepted: 12 March 2024 / Published online: 3 May 2024
© The Author(s) 2024

Abstract

This paper presents a study on the enhanced performance of ballasted tracks through the implementation of geogrids. A series of large-scale direct shear tests and impact tests was conducted with three distinct types of geogrids. The behavior of ballast was evaluated in terms of shear stress–strain responses and stress concentration using stress sensing sheets. Additionally, a micromechanical analysis utilizing the discrete element method was simulated on ballast assemblies with different geogrid reinforcements. The shear stress–strain responses of ballast simulated from DEM are comparable with those measured from large-scale direct shear tests, indicating that the inclusion of geogrid can enhance the performance of ballast by increasing its shear strength, as well as reducing the vertical displacement and the load distribution with depth. Micromechanical analysis was performed to investigate the influences of geogrids on contact force distribution, coordination number and orientation of contact which could not be captured in a laboratory environment. The use of geogrids in ballasted tracks certainly shows promise for sustainable and efficient railway infrastructure, as evidenced by the experimental and DEM-based findings, offering valuable insights into optimizing track stability and longevity.

Keywords Ballast · Geogrid · DEM · Direct shear test

Introduction

Railways play an essential role in advancing urban and national development across the globe, offering efficient transportation for passengers and freight. The Australian railway system stands as one of the world's most extensive, encompassing over 33,000 route kilometers of rail lines that traverse the nation, catering to urban as well as rural regions. The rising demand for railway services has presented new challenges, as increased train frequency, heavier loads, and

higher speeds have strained the existing infrastructure [1]. Consequently, the cost of maintaining Australia's railway tracks has surged, primarily attributed to ballast and regular substructure maintenance. Presently, the majority of Australian rail tracks need to be maintained and upgraded regularly to meet the growing demand, emphasizing the urgent need for innovative and sustainable solutions to enhance ballasted tracks [2]. These improvements are essential to accommodate faster, heavier, and longer trains, while ensuring passenger comfort and safety.

Geogrids, composed of synthetic materials such as polyester, primarily serve to reinforce rail track structures [3, 4]. These planar geogrids consist of parallel tensile ribs with opening apertures that secure and lock granular aggregates, effectively reducing the deformation of tracks [5, 6]. When integrated into ballasted tracks, geogrids offer confinement, preventing ballast from lateral movement, and subsequently diminishing track deformation [7, 8]. Past research has supported the efficacy of incorporating geogrids as an appropriate and cost-effective solution to mitigate ballast breakage, fouling, and track deterioration, underlining their importance in rail track applications [9–13], among others. Recently, experimental and

✉ Trung Ngo
Trung.Ngo@uts.edu.au

Buddhima Indraratna
Buddhima.Indraratna@uts.edu.au

¹ Transport Research Centre, School of Civil and Environmental Engineering, University of Technology Sydney, Ultimo, Australia

² Transport Research Centre, University of Technology Sydney, Ultimo, Australia

³ ARC Industrial Transformation Training Centre for Advanced Technologies in Rail Track Infrastructure (ITTC-Rail), Wollongong, Australia

DEM works on railways carried out by Naeini et al. [14] and Oskooei et al. [15] on recycled materials have demonstrated the application of recycled materials in tracks. Large-scale direct shear tests have been commonly adopted to study the effect of geogrids and recycled materials [16–20]. The performance of geogrids in rail tracks is influenced by several factors, including aperture shape and size, material stiffness, interface conditions, and grid placement location [21, 22]. Subgrade conditions can also impact the reinforcement effects provided by geogrids [23–25]. Among these factors, it is well accepted that the primary reason for the improved performance of the geogrid-stabilized ballast assembly is the geogrid–ballast interlocking [26–28].

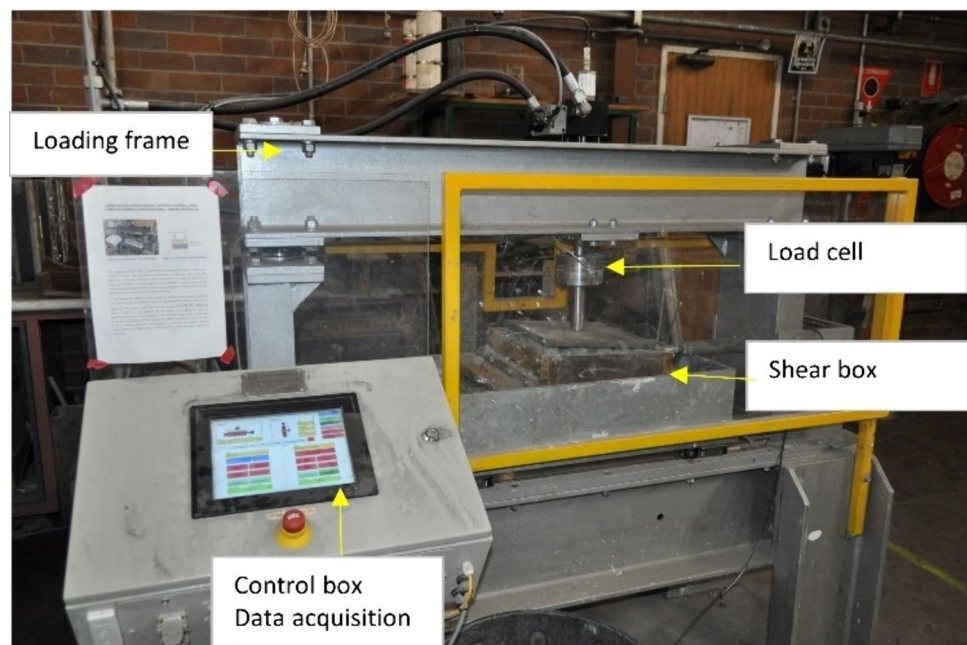
This paper presents results measured from large-scale direct shear tests and impact tests carried on ballast samples with and without the inclusions of different types of geogrid. In addition, three-dimensional discrete element modeling (DEM) using particle flow codes (PFC3D) is employed to simulate direct shear tests. The mechanism of the geogrid–ballast interaction subjected to direct shear loading was investigated from a micromechanical perspective. It is expected that the results obtained from the DEM simulations would provide more insightful understanding of the ballast–geogrid interface behaviour with respect to shear stress–strain responses, contact force distribution, coordination number, and orientation of principal contact forces under direct shear loading. It is noted that there have been other studies that address effects on train speeds and ride quality, and therefore, the effect of geogrids on train speeds and ride quality is not evaluated in this study.

Laboratory Tests

Large-Scale Direct Shear Tests

The large-scale direct shear box testing apparatus (Fig. 1) has dimensions of 300 mm width \times 300 mm length \times 200 mm height, and it was assembled in two equal halves to be used in laboratory testing. The upper box has the plan area dimensions of 300 mm \times 300 mm, and a height of 100 mm, while the lower box is longer by 100 mm to avoid the need for plan (cross-section) area correction during the shearing process (i.e., plan area of 400 mm \times 300 mm). The applied vertical stress is assumed to be uniformly distributed across the bottom box during shearing, as the contact area is unchanged. This apparatus can be used to perform both conventional constant normal load (CNL) and specialized constant normal stiffness (CNS) testing in fully automated mode. In the CNL testing (applied normal stress is kept constant during the test), normal stress as high as $\sigma_n = 500$ kPa can be applied over a range of horizontal strain rates. In this study, a series of conventional direct shear tests was conducted subjected to 3 normal stresses of $\sigma_n = 27$ kPa, 50 kPa, and 100 kPa. The loading was applied through a heavy-duty load cell (capacity of up to 500 kPa) powered by a high-capacity hydraulic pump (Fig. 1). A load cell was connected to an electronic datalogger to control a constant normal load during the shearing process and the position of load cell was monitored to measure the vertical displacement of the tested sample (dilation or compression responses). An additional calibrated load cell was horizontally affixed to measure the shear force at various shear displacements. During the test,

Fig. 1 Large-scale direct shear test used in the laboratory



the lower part of the shear box was horizontally displaced at a speed of 1.5 mm/min, while the upper section remained stationary. Each specimen was then subjected to a shear displacement of $\Delta_h = 60$ mm, corresponding to a shear strain of $\epsilon_s = 20\%$.

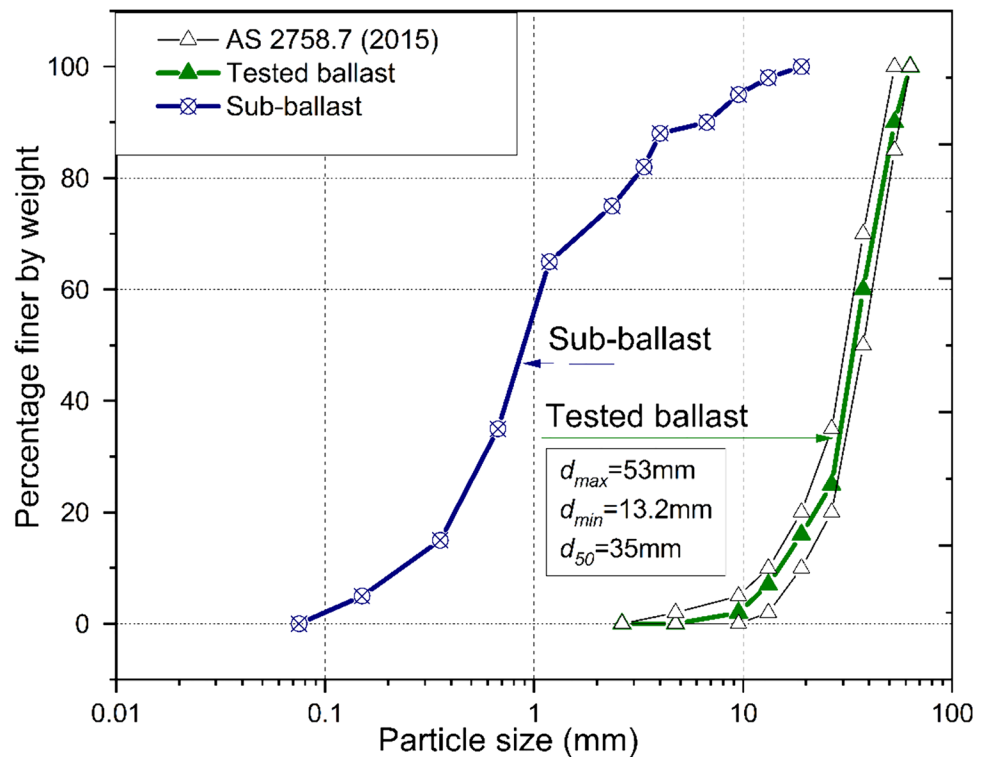
Fresh latite basalt collected from Bombo quarry in Kiama, NSW, Australia was chosen as tested ballast in laboratory following Australian Standards, AS 2758.7 (2015), as shown in Fig. 2. This ballast is hard and highly angular making them suitable for withstanding the cyclic loads from moving trains. The aggregates were painted in color to assist in visually observing ballast breakage after testing. Large-scale direct shear tests were carried out on ballast aggregates with and without the inclusion of geogrids. The aggregates were filled in the shear box and compacted into layers using a handheld compactor to the prescribed dry unit weight of 15.5–16.0 kN/m³ (initial void ratio, $e_0 = 0.74$; specific gravity, $G_s = 2.71$) to simulate the typical field density attained by vibratory tamping of heavy-haul tracks in most states of Australia. These results indicate that compaction alone cannot stabilize the ballast layer, because, to reduce lateral movement of particles, the inclusion of geogrids is necessary. Subsequently, a layer of geogrid was placed and secured at the interface between the lower and upper boxes, as shown in Fig. 3. The geogrid was securely clamped on both sides of the box to ensure a non-displacement boundary at the shearing plane. Three different types of geogrids, having varied geometry and opening apertures [biaxial

geogrids: BG1 (32 mm × 32 mm), BG2 (65 mm × 65 mm), and triaxial geogrid TG3, aperture: 37 mm], were tested to assess the influence of opening size and geometry on the shear strength of ballast. These three types of geogrids were selected as they are commonly used by the Australian railway industry and were available for the authors for testing through suppliers for Sydney Trains. The remaining ballast was then added and further compacted to achieve the desired density until the final height of the sample was fixed at 200 mm. A top loading plate was then placed on the top surface of the ballast assembly. The dynamic actuator was adjusted to apply designed normal load onto the loading plate. Prior the testing, all instrumentations, load cells, and datalogger were carefully checked to ensure that all readings were recorded properly. Throughout the shearing process, the datalogger (CMA system) automatically recorded the shearing forces and vertical displacement of the top plate. Laboratory test results are used to calibrate and validate the DEM simulations carried out in this study.

Large-Scale Impact Tests

This section briefly discusses the performance of geogrids subjected to impact loading, which often occurs in real-life tracks due to the presence of ‘wheel flats’ caused by excessive wear, and rail corrugations or other track imperfections. Impact forces with high magnitudes but with short duration (i.e., P_1 forces as described by Indraratna et al.

Fig. 2 Particle size distribution of materials used in the laboratory tests



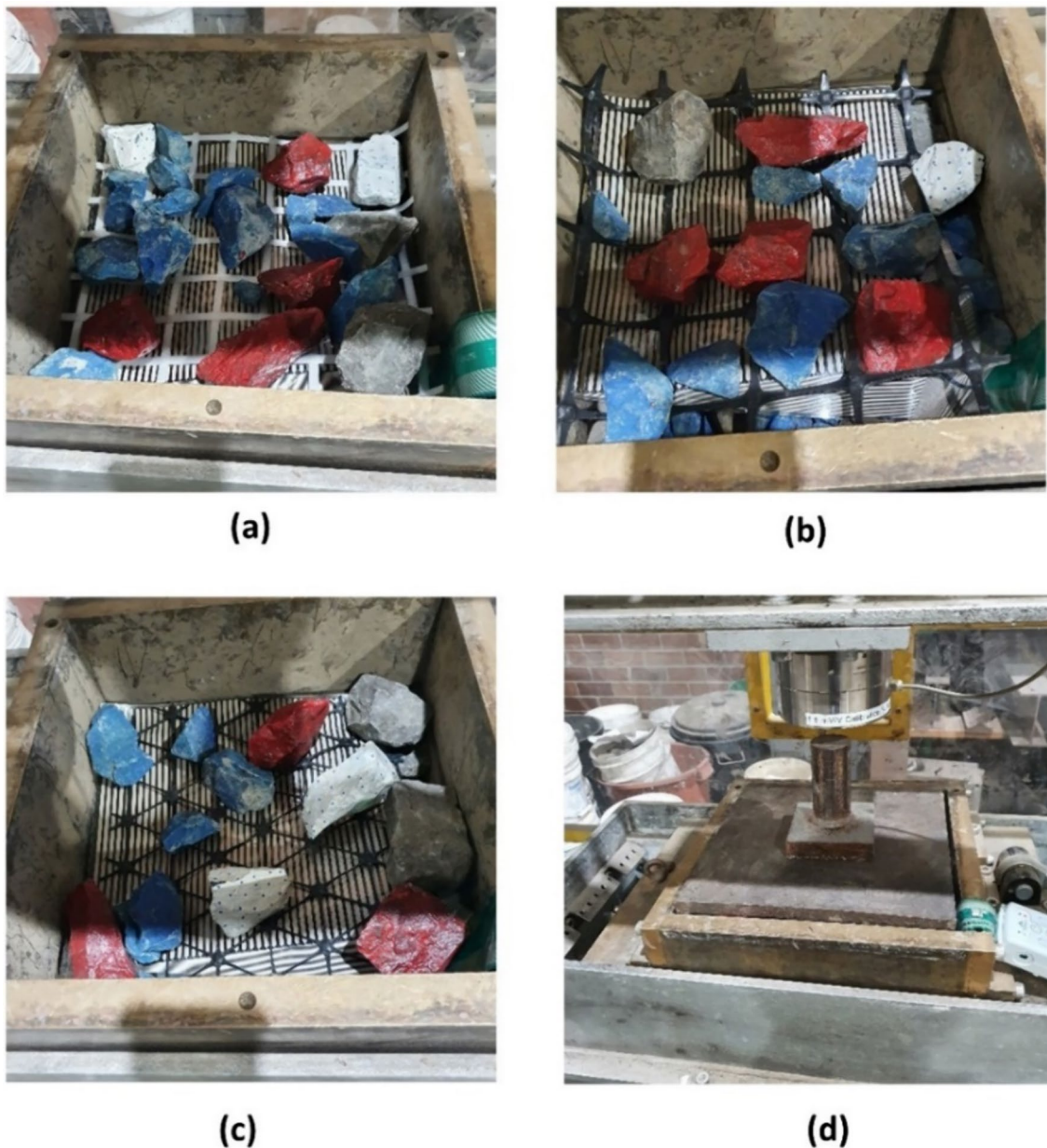


Fig. 3 Preparation of ballast sample with different geogrids: **a** BG1; **b** BG2; **c** Triaxial geogrid, TG3; and **d** ballast sample before shearing

[29]) cause significant ballast degradation and breakage. Considering the required brevity of the paper, a detailed testing program and results of large-scale impact tests have been described elsewhere by Indraratna et al. [29]. To assess the effect of geogrids under impact loads which occurring in real-life tracks [2], a drop weight impact testing apparatus having a free-fall hammer with a 5.81 kN weight, and released from a height of up to 6 m [30] was utilized to impose impact on ballast assemblies having a layer of geogrid. Figure 4 displays the impact testing facility and a standard test sample. The drop hammer was equipped with a load cell, and a piezoelectric

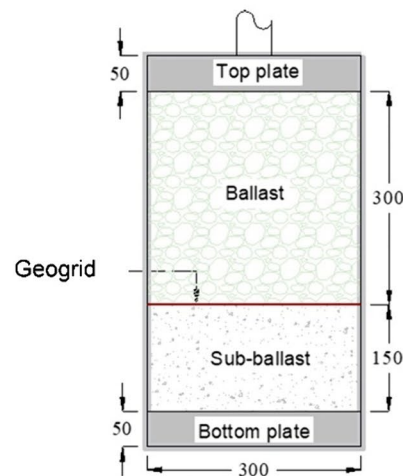
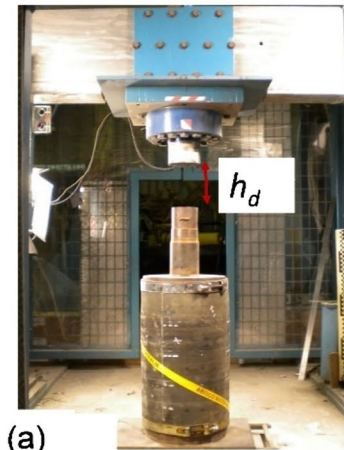
accelerometer to measure impact force and acceleration, respectively. The hammer was mechanically lifted to a specific drop height (h_d) and then released to apply impact forces onto the ballast specimen.

Ballast sample (diameter: 300 mm; height: 550 mm) was prepared within a cylindrical rubber membrane (thickness: 7 mm). At the base of the specimen, a 50 mm steel plate was placed, followed by a capping (100 mm) composed of a mixture of sand and gravel. Positioned above the capping layer, a layer of biaxial geogrid was set in place, followed by ballast (300 mm), as depicted in Fig. 4c. A 50 mm steel plate was then positioned atop the ballast layer to evenly distribute

Fig. 4 **a** Impact testing facility; **b** cross section of a ballast assembly with a geogrid; **c** placement of geogrid and ballast inside a cylindrical rubber membrane



Load cell attached to drop hammer



(b)



(c)

the load imposed by the descending hammer. It is noted that the subgrade effects are not studied in this current study.

Detailed testing program and results of the large-scale impact tests have been reported elsewhere by Indraratna et al. [29], where the main focus was on examining the effects of geogrid inclusions on impact forces, as well as the deformation and breakage of ballast. Measured test data highlighted that: (1) the utilization of a geogrid proved effective in diminishing both lateral and vertical deformations of the ballast, attributed to the reduced impact forces; (2) the average ballast breakage index (BBI)

was found to be lower when the geogrid was incorporated within the ballast compared to the scenario where no geogrid was applied; and (3) the measured acceleration indicated that the use of an artificial inclusion could significantly lower track vibrations and thereby mitigate the deformations and breakage of the ballast. From a practical standpoint, these findings suggest that the combination of geogrids and rubber mats has the potential to enhance safety and passenger comfort, while also offering the advantage of a more cost-effective track design that requires less maintenance.

Modeling of a Geogrid and Ballast in DEM

The discrete element method (DEM) is increasingly used in geotechnical engineering research projects as an alternative to the conventional finite element method (FEM). DEM allows for the examination of various aspects of ballast, including irregularly shaped grains, contact forces, particle breakage, interactions between particles and geogrids, among others [31–34]. These properties are often challenging to measure experimentally or with alternative continuum methods.

Modeling a geogrid in DEM presents a significant challenge due to the intricate geometry [35, 36]. In this study, three different types of geogrid were simulated by connecting multiple spheres (with radii ranging from 2.0 to 4.0 mm) through parallel bonds (Fig. 5). The strength of these bonds corresponds to the tensile strength of the geogrid and can be determined through tensile testing. Every bond delineates the

force–displacement characteristics of a finite-sized segment of cementitious material positioned between two spheres. These bonds establish an elastic interaction among particles, enabling the transmission of both forces and moments [37].

The moments and forces acting on parallel bonds are represented as \bar{M}_i and \bar{F}_i that can be broken down into their shear and normal components at contact points.

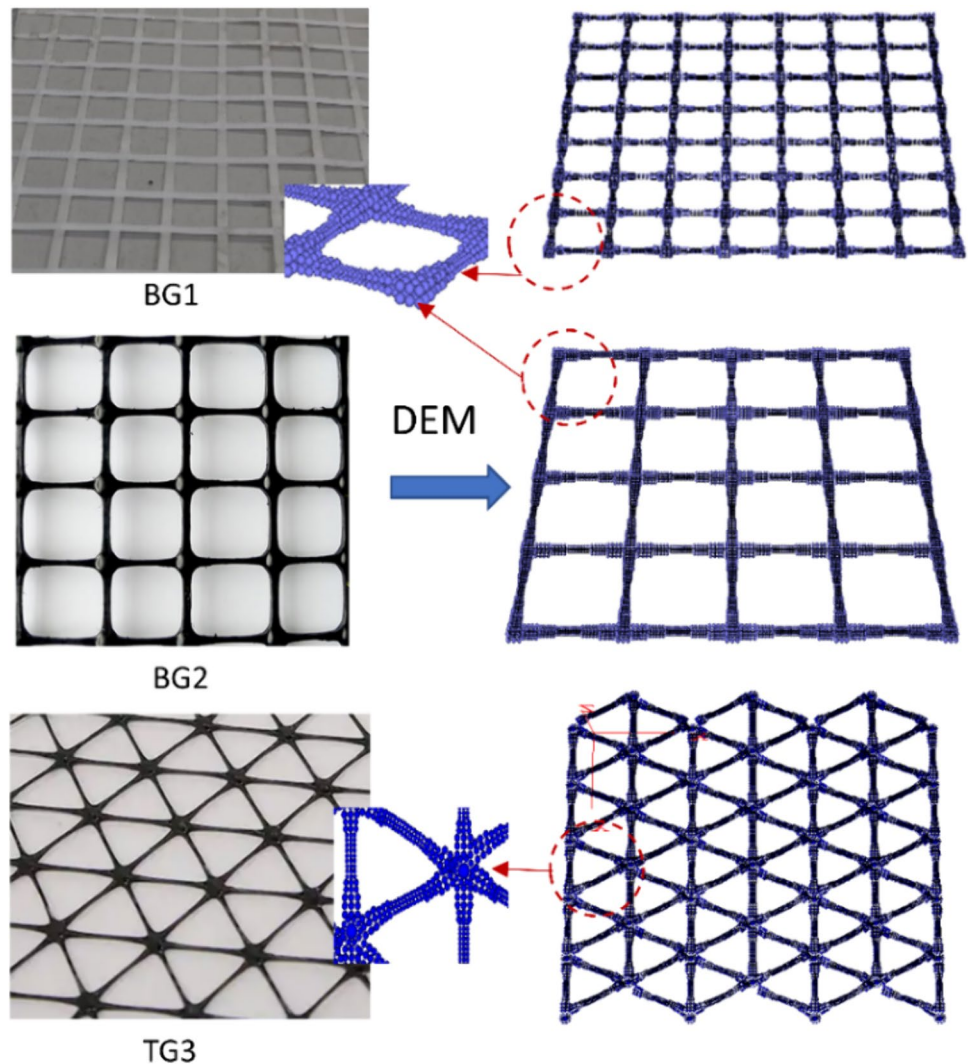
$$\bar{M}_i = \bar{M}_i^n + \bar{M}_i^s, \tag{1}$$

$$\bar{F}_i = \bar{F}_i^n + \bar{F}_i^s. \tag{2}$$

The incremental forces occur during a timestep, Δt are computed as:

$$\Delta \bar{F}_i^n = \left(-\bar{k}_n A \Delta U_i^n \right) n_i, \tag{3}$$

Fig. 5 DEM simulations for different types of geogrids



$$\Delta \bar{F}_i^s = -\bar{k}_s A \Delta U_i^s \tag{4}$$

The increment in moments are calculated by:

$$\Delta \bar{M}_i^n = \left(-\bar{k}_s J \Delta \theta_i^n \right) n_i, \tag{5}$$

$$\Delta \bar{M}_i^s = -\bar{k}_n I \Delta \theta_i^s, \tag{6}$$

where $\Delta \theta_i = \left(\omega_i^{[B]} - \omega_i^{[A]} \right) \Delta t$; ΔU_i^s and ΔU_i^n : relative increments of shear and normal displacements, respectively; $\Delta \theta_i^s$ and $\Delta \theta_i^n$: relative increments of shear and normal rotations; J , A , and I are: polar moment, area, and moment of inertia of the bond cross section, and they can be determined by:

$$J = \frac{1}{4} \pi R^4; A = \pi R^2; \text{ and } I = \frac{1}{2} \pi R^4. \tag{7}$$

The maximum shear stress and normal stress acted on the parallel bond can be calculated by:

$$\tau_{\max} = \frac{\left| \bar{F}_i^s \right|}{A} + \frac{\left| \bar{M}_i^n \right|}{J} \bar{R}, \tag{8}$$

$$\sigma_{\max} = \frac{-\bar{F}_i^n}{A} + \frac{\left| \bar{M}_i^s \right|}{I} \bar{R}. \tag{9}$$

If either of these maximum stresses surpasses its respective tensile strength, the parallel bond breaks, leading to the geogrid breaking.

Given that the engineering properties and mechanical behaviour of ballast are influenced by many factors including grain size, shape, and angularity, this study had employed a 3D laser scanner (VIVID 910) to scan the actual shape of particles. The process involved scanning randomly selected ballast grains to create polygonal meshes. Subsequently, sub-routines were programmed in the FISH language to construct particles within the DEM framework by connecting multiple spheres to fill the mesh, as illustrated in Fig. 6a.

Replicating the laboratory procedure, a DEM model representing a direct shear box is simulated in DEM (Fig. 6b). A geogrid layer was positioned at the middle of the shear box, followed by the placement of ballast aggregates (Fig. 6c–d). Initially, the lower portion of the shear box was filled with particles to meet the specified density requirements. Then, the remaining aggregates were filled on the top half of the shear box. Normal loads were applied on the top loading plate. The lower section of the shear box was subjected to strain-controlled loading and was sheared up to horizontal displacements of $\Delta_h = 60$ mm. This was achieved by applying a small velocity of the bottom walls (1×10^{-7} m/step). Throughout the simulation, the positions of the top loading plate, the displacements of the walls, and forces on vertical

walls were automatically regulated through a servo mechanism through the FISH program [37].

Determination of Micromechanical Parameters

Micromechanical parameters of materials are typically calibrated by leveraging known material responses observed at a macro scale. In this study, parameters of geogrid were calibrated using tensile tests (INSTRON apparatus) using the ASTM Standard D6637 (2011). Measured tensile load–displacement data were used for calibration with DEM simulations of the geogrid’s tensile test. By calibrating with experimental results, micromechanical parameters for geogrid were established and are listed in Table 1.

The micromechanical parameters for ballast were determined by calibrating the shear stress–strain responses, referencing laboratory tests previously conducted by the authors [1, 38]. Stiffness of ballast was determined through compression tests on rock samples. The parameters were adjusted interactively to match with experimental measurements, as presented in Table 1. Using the calibrated micromechanical parameters, the large-scale, direct shear testing of ballast reinforced by the geogrids was simulated in DEM to investigate the geogrid–ballast interaction from a micromechanical point of view.

Results and Discussion

Shear Stress–Strain Responses

Figure 7 presents a comparison of shear stress versus shear displacement obtained from DEM simulations with those measured in the experimental setting subjected to a normal stress of $\sigma_n = 50$ kPa. In general, there is a good match between the prediction and measured data proving that the DEM model effectively replicated the stress–strain responses of ballast reinforced by geogrids. In all simulations, the strain-softening of ballast is measured. The DEM simulations confirm that incorporating geogrid led to a rise in the maximum shear stress (shear strength) within geogrid-reinforced ballast assemblies, as expected. While the geogrid, BG1 provides only a marginal improvement in the shear strength of ballast, the inclusion of BG2 and TG3 exhibits a more pronounced improvement. This increase can be credited to the way ballast locks into the openings or apertures within the geogrid.

Figure 8 shows the comparison of predicted vertical displacement versus shear displacement between DEM and laboratory tests. The results clearly demonstrate that the ballast assemblies exhibit an initial compression of up to a shear displacement, Δ_h of around 5–7 mm, followed by dilation toward the end of the shearing process. The results also show

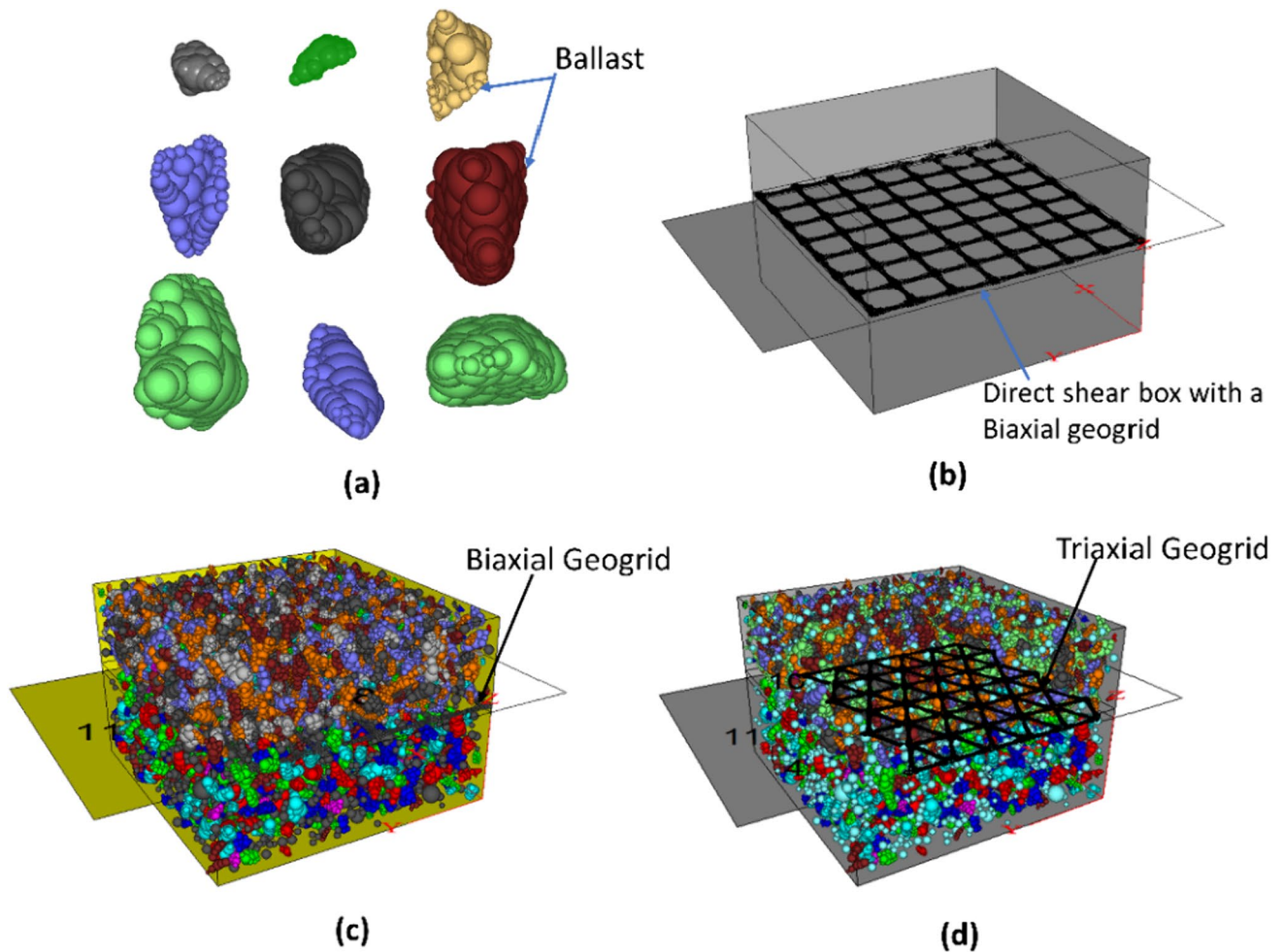


Fig. 6 DEM simulations of direct shear tests: **a** library of ballast shape; **b** direct shear box with a geogrid; **c** ballast assembly with a BG2; **d** ballast assembly with a TG3

Table 1 Micromechanical properties of geogrid and ballast adopted for DEM

Parameters	Geogrid	Ballast
Particle density (kg/m ³)	850	2500
Coefficient of friction	0.45	0.85
Contact normal stiffness, k_n (N/m)	4.68×10^6	6.84×10^7
Contact shear stiffness, k_s (N/m)	2.34×10^6	3.42×10^7
Contact normal stiffness of wall-particle, k_{n-wall} (N/m)	1×10^7	1×10^8
Shear stiffness of wall of wall-particle, k_{s-wall} (N/m)	1×10^7	1×10^8
Parallel bond radius multiplier, r_p	0.5	
Parallel bond normal stiffness, k_{np} (kPa/m)	6.42×10^7	
Parallel bond shear stiffness, k_{sp} (kPa/m)	3.21×10^7	
Parallel bond normal strength, σ_{np} (MPa)	386	
Parallel bond shear strength, σ_{sp} (MPa)	343	

that ballast reinforced with geogrids exhibits a decreased dilation when compared to unreinforced ballast. The reduction in dilation can be attributed to the mechanical interlocking occurring at the interface between the ballast and the geogrid that would create a non-displacement boundary condition, which minimizes the deformation of ballast.

Compared to laboratory test results, the DEM simulations exhibit a notable discrepancy in the predicted dilation that occurred after a shear displacement of about 10 mm. This divergence from accuracy could be attributed to the inability of the DEM analysis adopting spherical particle clusters to adequately capture the highly angular ballast aggregates and

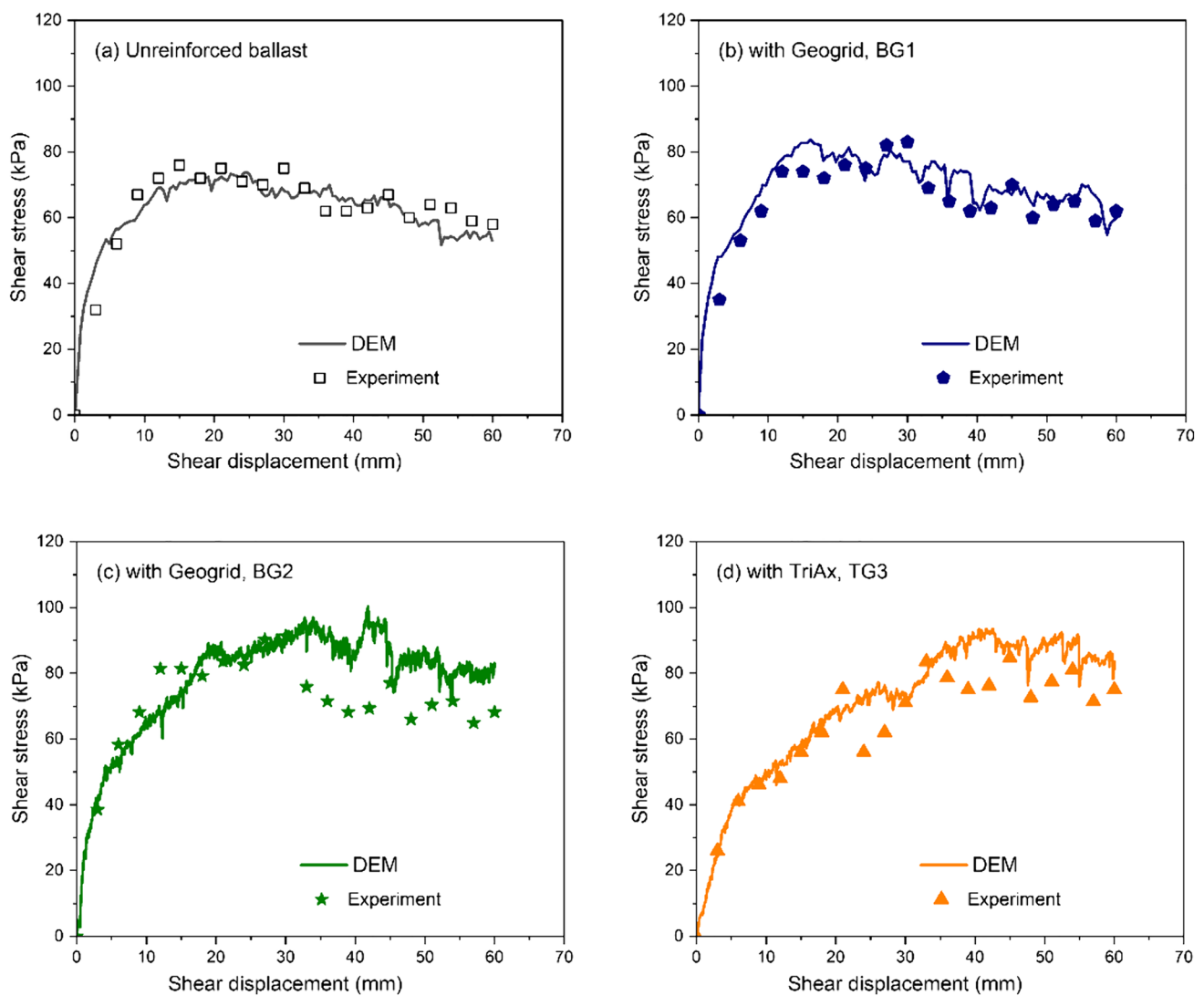


Fig. 7 Comparison of shear stress versus shear displacement between DEM and laboratory under 50 kPa normal stress: **a** without geogrid; **b** with BG1; **c** with BG2; and **d** with TG3

some particle breakage was not accurately captured in the current DEM analysis.

Measured Stress Distributions

In laboratory, a stress sensing sheet (SSS), 300 mm width \times 300 mm length, and 0.1 mm thickness was used to measure stress concentrations and contact areas of ballast in the shear box. The SSS is based on a surface sensor, comprising two thin layers with rows and columns of conductive silver (Fig. 9a). Sensor types vary in the spacing between consecutive rows or columns, typically ranging from 0.6 to 17 mm. In this approach, a pressure-sensitive semiconductor material is usually applied to the internal surface of silver rows and columns, sandwiched between two sheets to create a grid (matrix). As the SSS undergoes loading, the

upper sensor sheet is forced to make good contact with the lower sheet. The electrical resistance produced at the point where rows and columns intersect varies inversely with the magnitude of the applied normal force, which is then used to calculate stress concentration. The stress sensing sheet is thin (0.1 mm thick) and flexible; thereby, the effect on the interface shear behaviour between ballast and geogrids due to these stress sheets can be neglected. The SSS was connected to a computer installed with I-Scan software for data measurement (Fig. 9b).

Figure 10 shows the measurement of stress concentration contours beneath the ballast layer under normal stress of $\sigma_n = 100$ kPa and after a shear displacement of $\Delta_h = 10$ mm for tests conducted with and without the inclusion of geogrids. It is evident that the unreinforced ballast (without geogrid) exhibits numerous high-stress

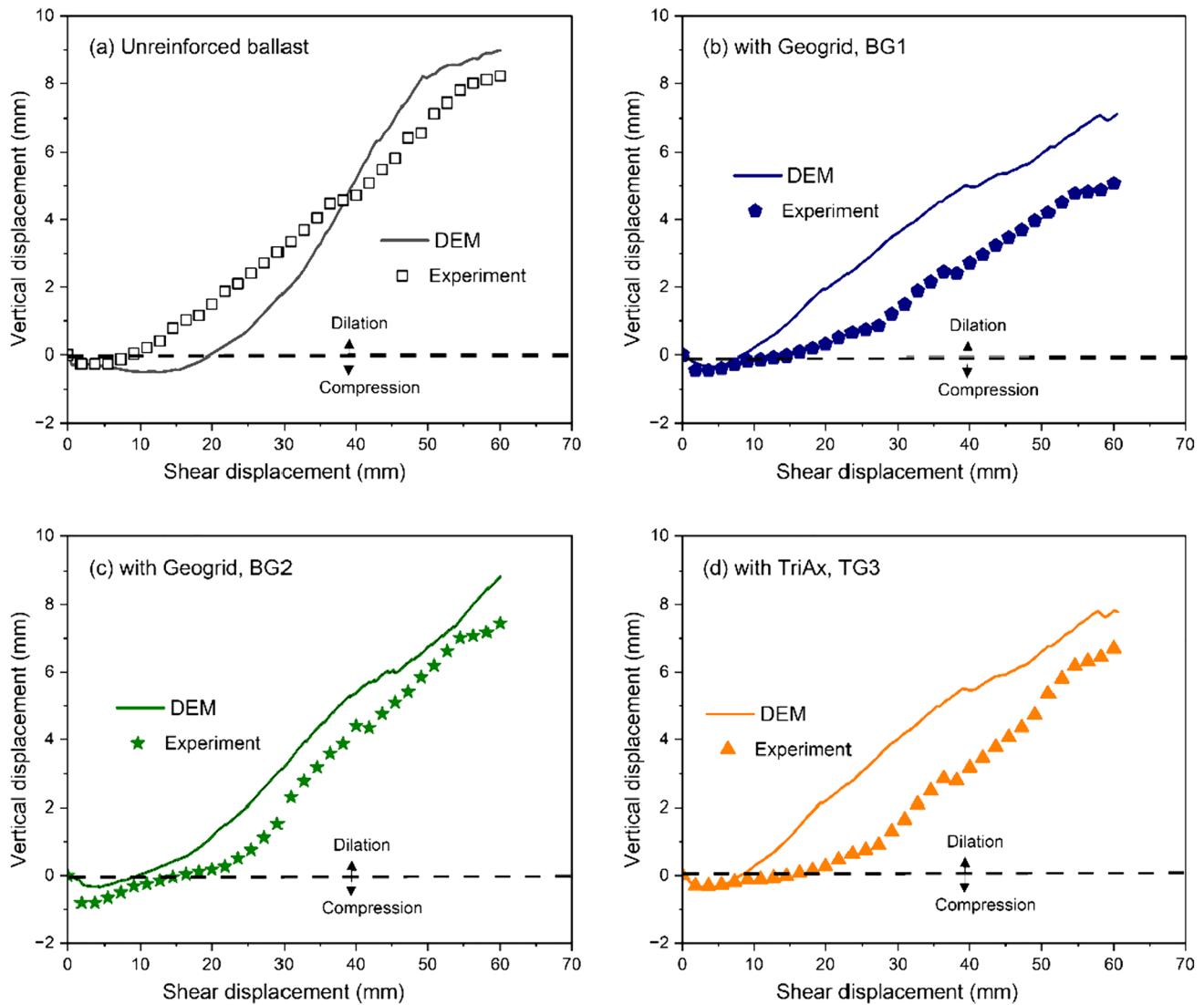


Fig. 8 Comparison of vertical displacement versus shear displacement between DEM and laboratory: **a** without geogrid; **b** with BG1; **c** with BG2; and **d** with TG3

concentration points (Fig. 10a), which had directly contributed to ballast breakage. In contrast, the inclusion of geogrids had resulted in a significant reduction of stress concentration points which could be associated with the increased contact areas (Fig. 10b–d). The reduction in stress concentration results in decreased ballast breakage, as observed in the laboratory [1]. When a triaxial geogrid, TG3 was placed in the ballast layer, there is a limited stress concentration and this could be attributed to the multi-directional load distribution capacity of the TG3, which allows for a more uniform stress distribution across the ballast assembly.

Contact Force Distribution

When subjected to shearing load, a network of contact force chains forms among the ballast particles and geogrids. This network is responsible for withstanding the applied shearing loads and transferring them across ballast assemblies. The distribution and orientation of these contact forces vary depending on the magnitude of the applied loads, and this directly influences the strength and deformation of materials, as described by Oda and Iwashita [39], and further investigated by Guo and Zhu [40], Yimsiri and Soga [41], among others. Altuhafi and Coop [42] demonstrated that the

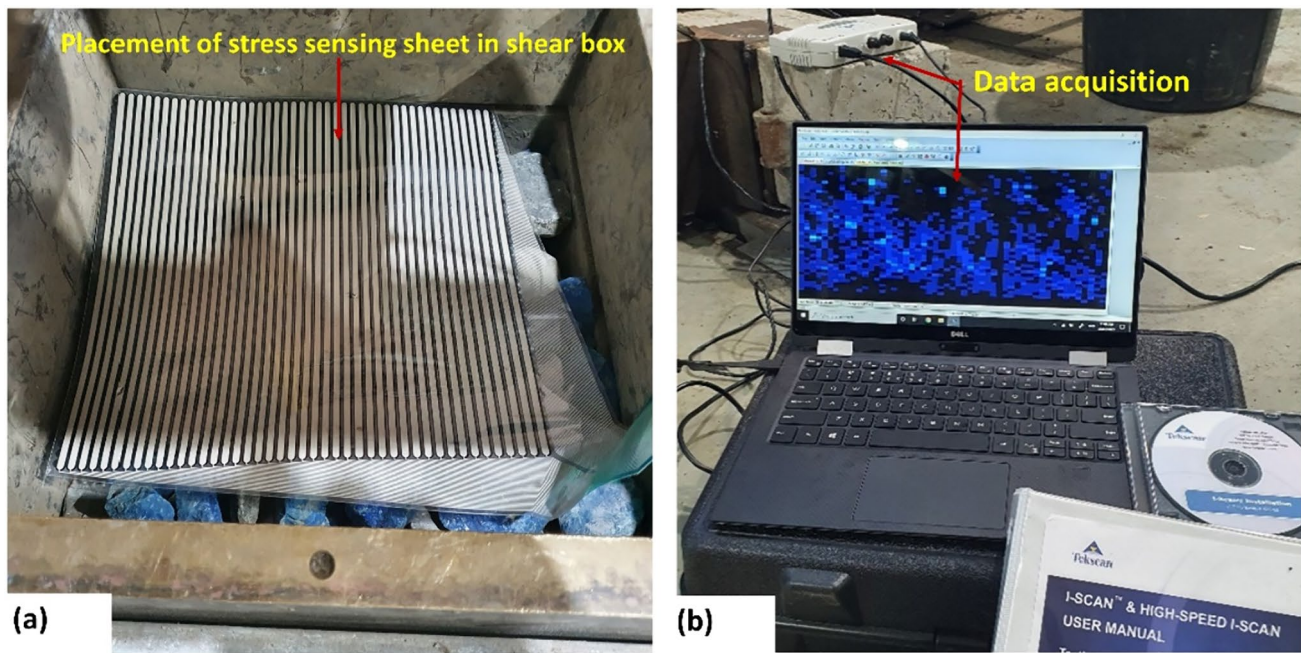


Fig. 9 **a** Placement of a stress sensing sheet in shear box; **b** data acquisition unit

degree of particle breakage relies not solely on the strength of the particles but also on the contact forces and particle arrangement. Figure 11 shows the mobilized contact force chains in ballast assemblies with and without the inclusion of geogrids under a normal stress, $\sigma_n = 100$ kPa captured from the DEM simulation. It is seen that the distribution of forces is non-uniform; varying across the ballast assembly having more contact forces forming in the region of ballast-geogrid interfaces. The number of contacts (N_{contact}) and the maximum contact forces (F_{max}) change with the inclusion of geogrids. When a geogrid is introduced, it reduces the maximum contact forces, because of its ability to absorb the applied shearing forces by mobilizing the geogrid's tensile strength. This results in reduced forces being transmitted to the ballast aggregates. For all simulations, the maximum contact forces were found to occur within the granular assembly, i.e., between ballast aggregates. The maximum mobilized tensile forces were different among the different geogrids, whereby the biaxial geogrid (BG1) exhibited the highest tensile force.

To shed more insight into the micromechanical implications of ballast-geogrid interaction, the changes in the number of contacts (N_{contact}) and maximum contact forces (F_{max}) predicted by DEM for ballast assemblies with and without the inclusion of geogrids, are presented in Fig. 12. It is predicted that the inclusion of geogrids leads to a significant increase in N_{contact} , while decreasing the maximum contact forces (F_{max}). When a geogrid is positioned in the middle of the shear box, the applied forces are not solely

transmitted through the large aggregate skeleton; they also transmitted across to the geogrid. This leads to a decrease in the maximum magnitude of contact force (i.e., with geogrid: $F_{\text{max}} = 542, 562,$ and 522 N with inclusion of BG1, BG2, and TG3, respectively). In contrast, $F_{\text{max}} = 754$ N without the inclusion of a geogrid, while having smaller number of contacts. The substantial interlocking between the geogrid and ballast had increased N_{contact} and subsequently mitigated the impact of large contact forces, thus effectively reducing the deformation of ballast. Consequently, particle breakage is minimized due to the reduction in the intensity of contact forces concentrated within the ballast matrix, as measured in the laboratory and field observations [2]. This micro-level DEM analysis offers valuable insights into the impact of geogrid, insights that are often challenging to obtain through laboratory testing.

Coordination Number

The coordination number (C_n) plays a crucial role in characterizing how particles are packed together on a microscopic level. It can be calculated based on the total number of contacts (N_{contact}) and particles (n_p) has within a given volume [31], as given by:

$$C_n = \frac{2N_{\text{contact}}}{n_p} \quad (10)$$

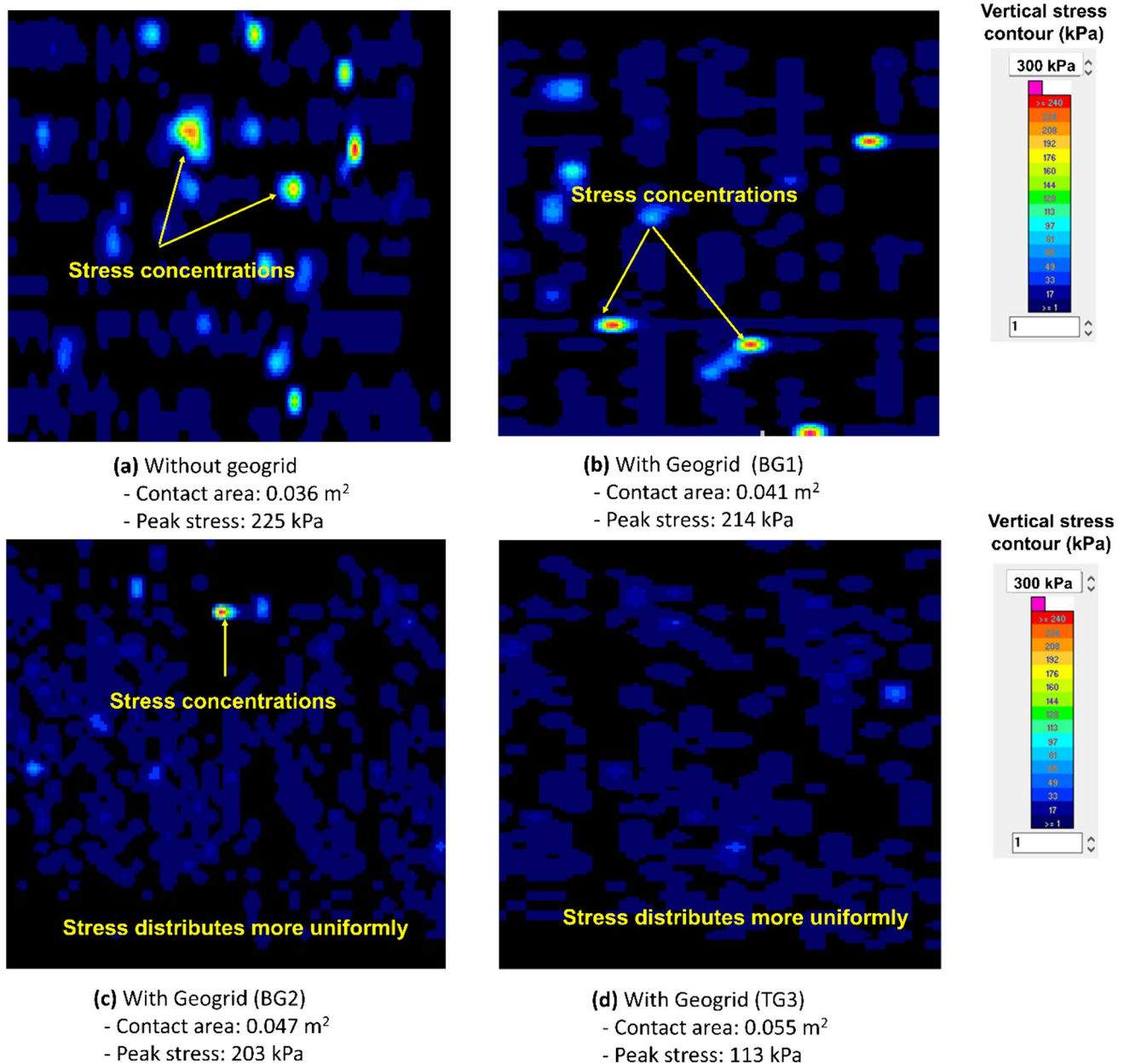


Fig. 10 Measurement of stress concentration and contact areas: **a** without geogrid; **b** with BG1; **c** with BG2; and **d** with TG3

The variation in C_n serves as an indicator of the gain or loss of particle contacts and is influenced by changes in packing density and interlocking among particles, during which new contacts are formed or particles break apart. Hasan and Alshibli [43] have demonstrated that the value of C_n is closely linked to the networks of contact forces and the ability of a granular assembly to carry a load. Todisco et al. [44] indicated that particles subjected to a higher C_n value are less likely to undergo breakage.

Based on the current DEM analysis, the evolutions of coordination number (C_n) are presented in Fig. 13. It is observed that at the beginning of the shearing stage, the

value of C_n increases and reaches a peak at the shear displacement of around $\Delta_h = 10\text{--}15$ mm, corresponding to the initial compression of ballast assemblies, followed by dilation at a later stage. The increase in C_n reflects particle rearrangement and densification to withstand the applied shearing load. As the shearing progresses, a strain-softening behavior was observed and this is reflected by a subsequent reduction in C_n . While the TG3-reinforced ballast assembly shows the highest values of coordination number ($C_n = 5.6\text{--}9.4$), the unreinforced ballast reveals the lowest values of C_n varying from 3.5 to 6.2. It is also observed that there are some fluctuations in C_n and this could be attributed

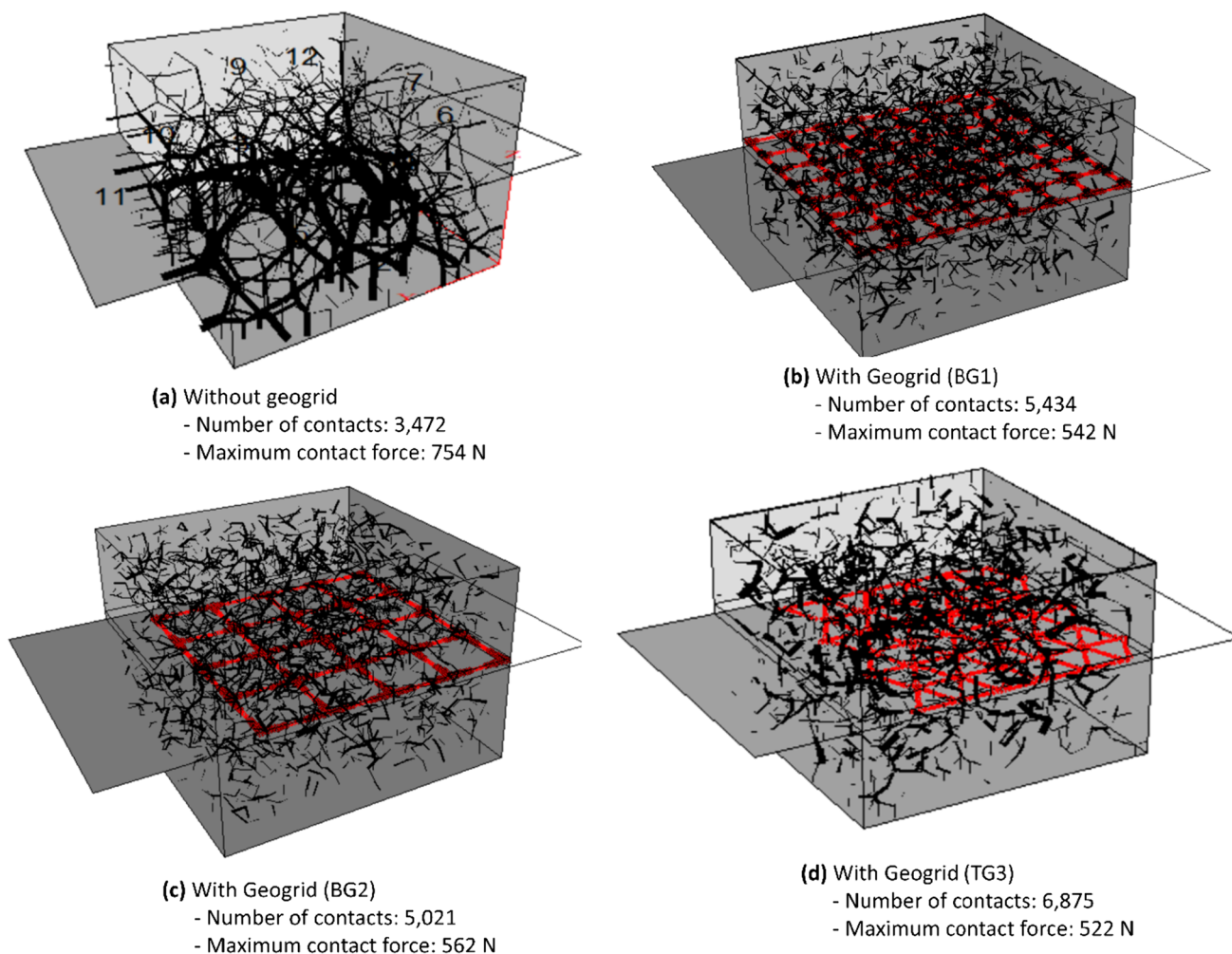


Fig. 11 Mobilised contact force chains in ballast assemblies: a without geogrid; b with BG1; c with BG2; and d with TG3

to the loss of interlocking between ballast and geogrid as well as breakage causing the particles to be re-arranged, thus forming new contacts to support the induced shearing load.

Orientation of Contacts

To examine the effect of geogrids has on the distribution of inter-particle contact forces in the ballast assembly, the orientation of contact forces is analyzed. A spatial space of a polar histogram was divided into 36 evenly sized bins, each with a bin angle of 10°. Contact force vectors, $F(\omega_i)$, located within each bin are collected to compute the distribution density, $P(\omega_i)$ of inter-particle contact forces within that specific bin, as described by the following equation [45]:

$$P(\omega_i) = \frac{\sum F(\omega_i)}{N_{\text{contact}} F_{\text{ave}}}, \tag{11}$$

where N_i is the number of inter-particle contacts in the i -th bin, F_{ave} is the averaged contact force. Fourier analysis was then carried out on the $P(\omega_i)$ using the methods outlined by Bathurst and Rothenburg [45] to quantify the anisotropy of inter-particle contact forces, as expressed by:

$$F(\theta_i) = 1 + a \cos 2(\theta_i - \theta_r) + b \cos 4(\theta_i - \theta_r), \tag{12}$$

where $F(\theta_i)$ is the distribution density of inter-particle contact force at the orientation angle of θ_i ; a , b , and θ_r are fitting parameters, and θ_r representing the principal orientation of inter-particle contact force.

Figure 14 presents a polar histogram of inter-particle contact forces for the four ballast assemblies under $\sigma_n = 50\text{kPa}$ captured at a shear displacement of $\Delta_h = 10\text{ mm}$. It is noted that the inter-particle contact forces are predominantly distributed in vertical direction to support the self-weight of ballast as well as the applied normal stress. The unreinforced ballast assembly has a principal orientation of inter-particle

Fig. 12 Variation of number of contacts, $N_{contact}$ and maximum contact forces, F_{max} of ballast with and without the inclusion of geogrids

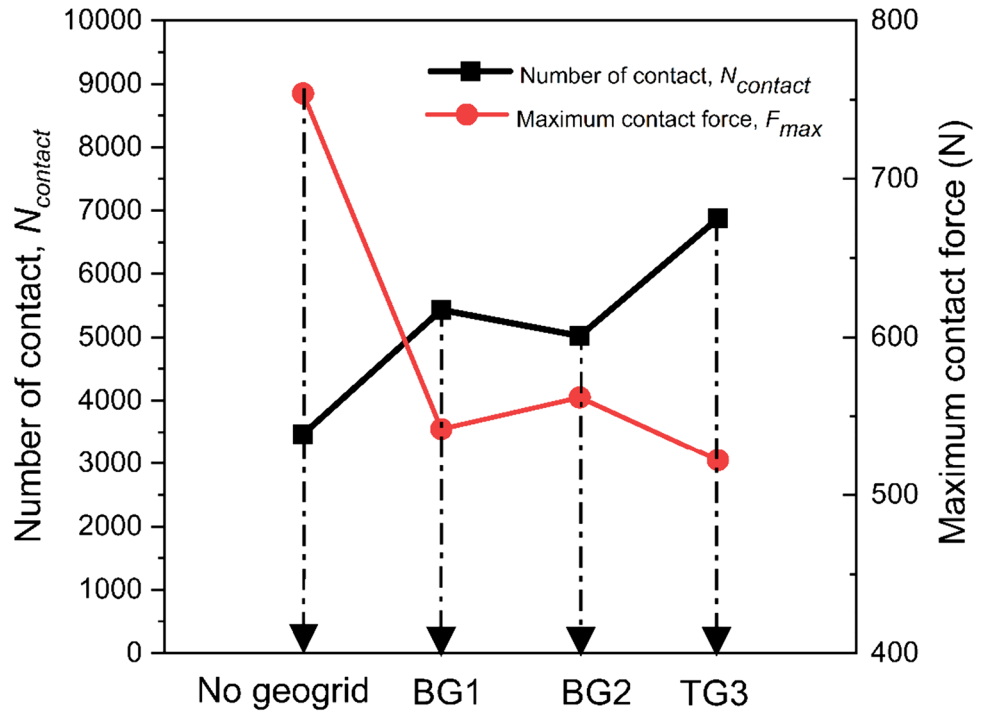
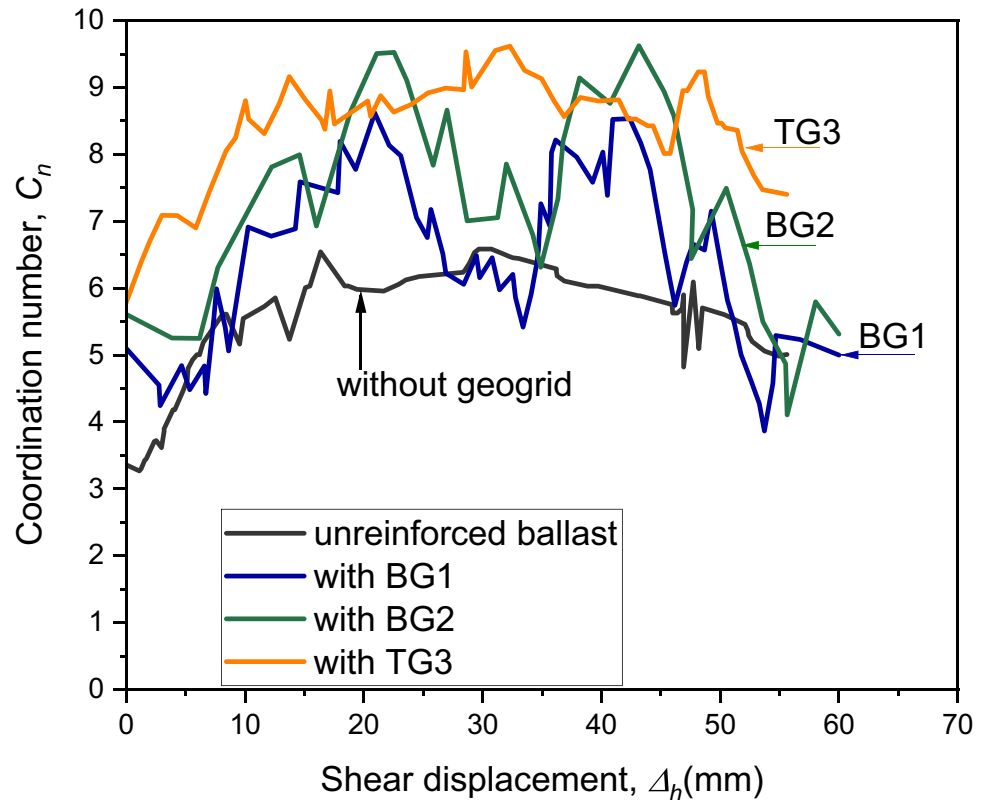


Fig. 13 Evolutions of coordination number, C_n during the shearing progress



contact force of $\theta_r = 7^\circ$. In contrast, the geogrid-reinforced ballast assemblies have a much higher of principal orientation of $\theta_r = 13^\circ, 21^\circ$, and 18° for BG1, BG2, and TG3, respectively. The inclusion of geogrid resulted in increased

principal orientation of contact toward horizontal plane; and this is attributed to more contacts are formed through the interlocking of ballast aggregates and geogrids. It is noted that the current micromechanical modeling using DEM

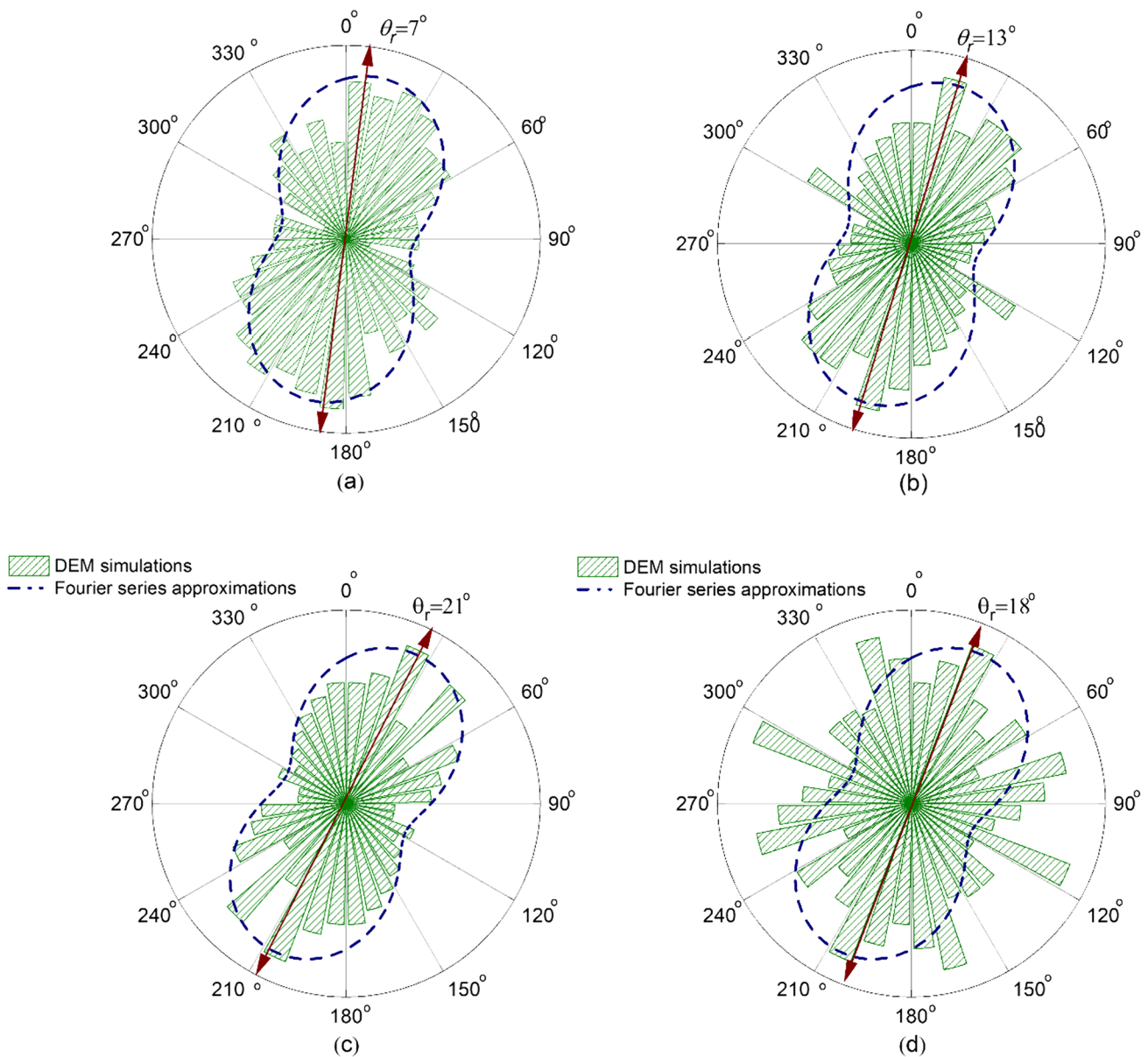


Fig. 14 Polar histograms of inter-particle contact forces for ballast assemblies with different geogrid reinforcement at $\Delta_h = 10\text{mm}$: **a** unreinforced ballast; **b** with BG1; **c** with BG2; and **d** with TG3

has obvious limitations as the boundary conditions and the assembly of particle clusters do not perfectly mimic the field conditions. The micromechanical analysis was carried out based on actual information directly captured as outputs from DEM simulations, and there were no assumptions or simplifications required. The requirement of extensive computational resources is one of the challenges or limitations encountered in DEM analysis, and this is well-known within the geotechnical community. To reduce the computational time, a small model test is often simulated in DEM (i.e., reducing the number of particles within a manageable section of the problem), and this may result in some

discrepancies as the boundary conditions and particle clusters do not always mimic the field conditions perfectly.

Conclusions

The current study was primarily focused on understanding how the inclusion of geogrids affects the shear stress–strain responses and the performance of ballast subjected to direct shear loading in a micromechanical perspective. The study employed a combination of laboratory experiments and DEM modeling, which were conducted on ballast with

geogrid reinforcements. The salient findings of this study can be summarized as follows:

- The inclusion of geogrids significantly increased the shear strength and decreased the dilation of ballast under direct shear loading conditions. This was due to improved interlocking between the ballast and geogrid, resulting in a higher peak shear stress and a reduced particle displacement.
- DEM simulations proved that the geogrid could impart a higher value of N_{contact} as compared to the unreinforced one. This results in a reduced maximum contact force, F_{max} (with geogrid: $F_{\text{max}} = 542, 562, \text{ and } 522 \text{ N}$ with inclusion of BG1, BG2, and TG3). In contrast, without the inclusion of a geogrid, the maximum contact force was up to $F_{\text{max}} = 754 \text{ N}$. This finding implies that the applied forces are not solely transmitted through the large aggregate skeleton; they also transmitted to the geogrid and subsequently mitigate the impact of large contact forces, and thus effectively reducing track deformation.
- The inclusion of geogrid resulted in increased coordination number (C_n). Indeed, the unreinforced ballast has the lowest values of C_n varying from 3.5 to 6.2; the TG3-reinforced ballast assembly shows the highest values of coordination number ($C_n = 5.6\text{--}9.4$). The increase in C_n is reflected by the interlocking, facilitating the transmission of forces throughout the assembly.
- The analysis of contact orientations in both unreinforced and geogrid-reinforced ballast assemblies during shearing revealed that particles were re-arranged and rotated to support induced loads. With the inclusion of a geogrid, contact forces were redistributed and reoriented, aligning more toward the horizontal shearing direction to support the applied shear loads.

In a practical sense, based on the outcomes of laboratory testing and DEM simulations executed in this study, it can be concluded beyond doubt that the use of geogrids holds the potential for significantly improving the performance of ballast on a rail track, offering valuable insights into optimizing track stability and enhancing track longevity. A coupled DEM–FEM solution for analyzing real-life track sections supported by a field trial adopting distinctly different types of geogrids with varied aperture arrangements (e.g., square vs triangular) is recommended.

Acknowledgements This study was carried out by the Industrial Transformation Training Centre for Advanced Technologies in Rail Track Infrastructure (ITTC-Rail), funded by the Australian Research Council, ARC (IC170100006) and the ARC Discovery Project (DP220102862). The Authors are grateful to Mr. Cameron Neilson (UOW) for the assistance during the laboratory tests.

Author Contributions TN: Validation, Investigation, Writing—original draft, Data analysis and interpretation, Formal analysis,

Writing—review and editing. BI: Conceptualization, Supervision, Investigation, Funding, Project administration, Writing—review and editing.

Funding Open Access funding enabled and organized by CAUL and its Member Institutions. Australian Research Council, Projects: IC170100006; DP220102862.

Data Availability The datasets used and/or analyzed during the current study are available from the corresponding author on reasonable request.

Code Availability Not applicable.

Declarations

Conflict of interest The authors declare that they have no known competing financial interests or personal relationships that could have appeared to influence the work reported in this paper.

Open Access This article is licensed under a Creative Commons Attribution 4.0 International License, which permits use, sharing, adaptation, distribution and reproduction in any medium or format, as long as you give appropriate credit to the original author(s) and the source, provide a link to the Creative Commons licence, and indicate if changes were made. The images or other third party material in this article are included in the article's Creative Commons licence, unless indicated otherwise in a credit line to the material. If material is not included in the article's Creative Commons licence and your intended use is not permitted by statutory regulation or exceeds the permitted use, you will need to obtain permission directly from the copyright holder. To view a copy of this licence, visit <http://creativecommons.org/licenses/by/4.0/>.

References

1. Indraratna B, Rujikiatkamjorn C, Salim W (2023) Advanced rail geotechnology—ballasted track. CRC Press, London
2. Indraratna B, Nimbalkar S, Christie D, Rujikiatkamjorn C, Vinod JS (2010) Field assessment of the performance of a ballasted rail track with and without geosynthetics. *J Geotech Geoenviron Eng ASCE* 136(7):907–917
3. Shukla SK, Yin JH (2006) Fundamentals of geosynthetic engineering. Taylor & Francis Group, London
4. Bhardwaj A, Mittal S (2023) Enhancing stiffness behavior of railway embankment for high-speed tracks with geogrids. *Int J Geosynth Ground Eng* 9(5):64
5. Esmaili M, Naderi B, Neyestanaki HK, Khodaverdian A (2018) Investigating the effect of geogrid on stabilization of high railway embankments. *Soils Found* 58(2):319–332
6. Prashanth V, MuraliKrishna A, Dash SK (2016) Pullout tests using modified direct shear test setup for measuring soil-geosynthetic interaction parameters. *Int J Geosynth Ground Eng* 2(2):10
7. Desbrousses RLE, Meguid MA, Bhat S (2023) Experimental investigation of the effects of subgrade strength and geogrid location on the cyclic response of geogrid-reinforced ballast. *Int J Geosynth Ground Eng* 9(6):67
8. Brown SF, Kwan J, Thom NH (2007) Identifying the key parameters that influence geogrid reinforcement of railway ballast. *Geotext Geomembr* 25(6):326–335

9. Indraratna B, Ngo NT, Rujikiatkamjorn C (2011) Behavior of geogrid-reinforced ballast under various levels of fouling. *Geotext Geomembr* 29(3):313–322
10. Tutumluer E, Huang H, Bian X (2012) Geogrid-aggregate interlock mechanism investigated through aggregate imaging-based discrete element modeling approach. *Int J Geomech* 12(4):391–398
11. Luo Z, Zhao C, Cai W, Gu Q, Lin W, Bian X, Chen Y (2023) Full-scale model tests on ballasted tracks with/without geogrid stabilisation under high-speed train loads. *Géotechnique*, 1–15
12. Jia Y, Zhang J, Chen X, Miao C, DEM Zheng Y (2023) study on shear behavior of geogrid-soil interfaces subjected to shear in different directions. *Comput Geotech* 156:105302
13. Fischer S (2022) Geogrid reinforcement of ballasted railway superstructure for stabilization of the railway track geometry—a case study. *Geotext Geomembr* 50(5):1036–1051
14. Naeini M, Mohammadinia A, Arulrajah A, Horpibulsuk S (2021) Cyclic behavior of semi-rigid recovered plastic blends in railway track substructure. *Transp Geotech* 28:100514
15. Oskooei PR, Mohammadinia A, Arulrajah A, Horpibulsuk S (2021) DEM modeling and experimental analysis of the breakage behavior of recycled crushed brick particles. *Transp Geotech* 30:100586
16. Karnamprabhakara B, Balunaini U, Arulrajah A, Evans R (2023) Evaluation of interaction properties of uniaxial geogrids with waste foundry sand. *Geosynth Int* 30(2):169–183
17. Naeini M, Mohammadinia A, Arulrajah A, Horpibulsuk S, Leong M (2019) Stiffness and strength characteristics of demolition waste, glass and plastics in railway capping layers. *Soils Found* 59(6):2238–2253
18. Suddeepong A, Hoy M, Nuntasena C, Horpibulsuk S, Kantatham K, Arulrajah A (2022) Evaluation of interface shear strength of natural kenaf geogrid and recycled concrete aggregate for sustainable pavement applications. *J Nat Fibers* 19(13):6165–6181
19. Horvát F, Fischer S, Major Z (2013) Evaluation of railway track geometry stabilisation effect of geogrid layers under ballast on the basis of laboratory multi-level shear box tests. *Acta Tech Jaurinensis* 6(2):21–44
20. Orosz Á, Farkas Z, Tamás K (2023) Experimental investigation of mixing railway ballast grains with different form using large-scale direct shear box apparatus. *Transp Geotech* 42:101105
21. Bathurst RJ, Raymond GP (1987) Geogrid reinforcement of ballasted track. *Transp Res Rec* 1153:8–14
22. Brown SF, Selig ET (1991) The design of pavement and rail track foundation. Cyclic loading of soils: from theory to design. Blackie and Son Ltd, New York, pp 249–305
23. Shukla SK (2002) Geosynthetic applications—general aspects and selected case studies. *Geosynthetics and their Applications*. Thomas Telford Publishing, London, pp 393–419
24. Ferreira FB, Vieira CS, Lopes ML (2015) Direct shear behaviour of residual soil–geosynthetic interfaces—influence of soil moisture content, soil density and geosynthetic type. *Geosynth Int* 22(3):257–272
25. Choudhary AK, Krishna AM (2016) Experimental investigation of interface behaviour of different types of granular soil/geosynthetics. *Int J Geosynth Ground Eng* 2(1):4
26. McDowell GR, Harireche O, Konietzky H, Brown SF, Thom NH (2006) Discrete element modelling of geogrid-reinforced aggregates. *Proc ICE Geotech Eng* 159(1):35–48
27. Koerner RM (2005) Designing with geosynthetics, 5th edn. Pearson Prentice Hall, Upper Saddle River
28. Chen C, McDowell GR, Thom NH (2012) Discrete element modelling of cyclic loads of geogrid-reinforced ballast under confined and unconfined conditions. *Geotext Geomembr* 35:76–86
29. Indraratna B, Ngo T, Bessa FF, Rujikiatkamjorn C, Shahkolahi A (2020) Laboratory examination of ballast deformation and degradation under impact loads with synthetic inclusions. *Transp Geotech* 25:100406
30. Remennikov AM, Kaewunruen S (2014) Experimental load rating of aged railway concrete sleepers. *Eng Struct* 76:147–162
31. O’Sullivan C (2011) Particulate discrete element modelling: a geomechanics perspective. Spon Press, London
32. Potyondy DO, Cundall PA (2004) A bonded-particle model for rock. *Int J Rock Mech Min Sci* 41(8):1329–1364
33. Liu S, Qiu T, Qian Y, Huang H, Tutumluer E, Shen S (2019) Simulations of large-scale triaxial shear tests on ballast aggregates using sensing mechanism and real-time (SMART) computing. *Comput Geotech* 110:184–198
34. Orosz Á, Bagi K (2023) Comparison of contact treatment methods for rigid polyhedral discrete element models. *Int J Rock Mech Min Sci* 170:105550
35. Han J, Bhandari A, DEM Wang F (2011) analysis of stresses and deformations of geogrid-reinforced embankments over piles. *Int J Geomech ASCE* 12(4):340–350
36. Chen W, Zhang Y, Wang C, Xiao Y, Lou P (2023) Effect of ballast pockets and geogrid reinforcement on ballasted track: numerical analysis. *Transp Geotech* 42:101108
37. Itasca (2018) Particle flow code in three dimensions (PFC3D). Itasca Consulting Group Inc, Minnesota
38. Ngo NT, Indraratna B, DEM Rujikiatkamjorn C (2014) Simulation of the behaviour of geogrid stabilised ballast fouled with coal. *Comput Geotech* 55:224–231
39. Oda M, Iwashita K (1999) Mechanics of granular materials: an introduction. A. A Balkema, Rotterdam
40. Guo W-L, Zhu J-G (2017) Particle breakage energy and stress dilatancy in drained shear of rockfills. *Géotech Lett* 7(4):304–308
41. Yimsiri S, DEM Soga K (2010) Analysis of soil fabric effects on behaviour of sand. *Géotechnique* 60(6):483–495
42. Altuhafi FN, Coop MR (2023) The small-strain stiffness of a railway ballast. *Géotechnique*, 1–12
43. Hasan A, Alshibli K (2012) Three dimensional fabric evolution of sheared sand. *Granul Matter* 14(4):469–482
44. Todisco MC, Coop MR, Guo Q, Senetakis K (2015) The effect of the coordination number on particle crushing. In: International symposium on geomechanics from micro to macro, IS-Cambridge 2014. Taylor and Francis, Balkema, pp 1063–1068
45. Bathurst RJ, Rothenburg L (1992) Investigation of micromechanical features of idealized granular assemblies using DEM. *Eng Comput* 9:199–210

Publisher's Note Springer Nature remains neutral with regard to jurisdictional claims in published maps and institutional affiliations.